Numerical study of the turbulent transonic interaction and transition location effect involving optimisation around a supercritical aerofoil

Damien Szubert [a,*], Ioannis Asproulias [a], Fernando Grossi [a], Régis Duvigneau [b], Yannick Hoarau [c], Marianna Braza [a]

[a] *Institut de Mécanique des Fluides de Toulouse, UMR N° 5502 CNRS-INPT-UPS, Allée du Prof. Camille Soula, F-31400 Toulouse, France*

[b] *INRIA Sophia Antipolis - Méditerranée, ACUMES Team, France*

[c] *Laboratoire ICUBE, UMR N° 7357, Strasbourg, France*

A B S T R A C T

The present article analyses the turbulent flow around a supercritical aerofoil at high Reynolds number and in the transonic regime, involving shock-wave/boundary-layer interaction (SWBLI) and buffet, by means of numerical simulation and turbulence modelling. Emphasis is put on the transition position influence on the SWBLI and optimisation of this position in order to provide a maximum lift/drag ratio. A non-classical optimisation approach based on Kriging method, coupled with the URANS modelling, has been applied on steady and unsteady flow regimes. Therefore, the present study contributes to the so-called 'laminar-wing design' with the aim of reducing the drag coefficient by providing an optimum laminar region upstream of the SWBLI.

1. Introduction

The present study has been carried out in the context of the European research program TFAST, "Transition location effect on shock-wave/boundary-layer interaction", project No. 265455. One of the main objectives of this research is to provide optimal laminarity in the boundary layer upstream of the shock-wave/boundary-layer interaction (SWBLI), in order to reduce the skin friction comparing to the fully turbulent case and therefore reduce drag, in the context of greening aircraft transport (a major objective of the *Horizon 2020* European programme). Due to increased aerodynamic loads and aero-engine components nowadays, supersonic flow velocities are more frequent, generating shock waves that interact with boundary layers. Laminar shock-wave/boundary-layer interaction can rapidly cause flow separation, which is highly detrimental to aircraft performance and poses a threat to safety. This situation can be improved by imposing the laminar–turbulent transition upstream of the interaction, but this should be carefully done in order to keep the aerodynamic efficiency high (lift/drag ratio).

In the context of the European research program TFAST, several ways of controlling the position of the transition are carried out. To this end, a supercritical laminar wing, the so-called V2C, has been designed by Dassault Aviation. This profile allows the boundary layer to remain laminar up to the shock foot, even in the environment of transonic wind tunnels of the laboratories involved in the project, and up to the angle of attack of 7.0°. Experimental results for the present configuration are not yet available in the present research project. Regarding the related literature, the transonic buffet has been studied experimentally in detail since the 70s on circular-arc aerofoils [1,2], and most recently on supercritical aerofoils [3]. In this latest study, a fixed transition tripping was applied at 7% of the chord. The physics governing the transonic buffet is complex and several theories have been proposed, like the effect of the feedback mechanism of waves propagating from the trailing edge, or the onset of a global instability [3–5]. Comparison of numerical results by Deck [6], Grossi et al. [7] and Szubert et al. [5] with the experimental results by Jacquin et al. [8] concerning the transonic buffet around supercritical wings with fixed transition showed the predictive capability of recent CFD methods and a physical analysis of the interaction between buffet and trailing-edge instabilities. The SWBLI involving transonic buffet and laminar wing design currently highly interests the aeronautical industries (Cleansky European project, "Advanced, high aspect ratio transonic laminar wing" [9]). Laminar wing design in transonic regimes has been studied in respect of transition control by means of Discrete Roughness Elements (DRE's) [10]. Navier–Stokes simulations of transonic buffet as well as of the shock–vortex

* Corresponding author.
E-mail address: damien.szubert@imft.fr (D. Szubert).

http://dx.doi.org/10.1016/j.euromechflu.2015.09.007

interaction at moderate Reynolds numbers were reported by Bouhadji and Braza [11], as well as DNS by Bourdet et al. [12]. In the high Reynolds number range, typical of aerodynamic applications, the use of appropriate turbulence modelling is necessary. Concerning transonic buffet, the unsteady shock-wave/boundary-layer interaction represents a major challenge for turbulence models and the low frequencies associated with the shock-wave motion can make the simulations very expensive. Since the first simulations by Seegmiller et al. [2] and Levy Jr. [13] for a circular-arc aerofoil, Unsteady Reynolds-Averaged Navier–Stokes (URANS) computations using eddy-viscosity turbulence models have been largely used to predict the phenomenon over two-dimensional aerofoils. Pure LES simulations, even combined with specific wall-models, are yet quite costly for the high Reynolds number range of real flight configurations. For this reason, hybrid RANS–LES methods have been developed in the last decade and start to be largely used in the industrial context together with adapted, advanced URANS approaches. The hybrid methods combine the robustness and near-wall physics offered by URANS in the near region, as well as LES advantages in capturing the physics of unsteady vortices and instabilities development in the detached flow regions. Among the hybrid methods, the Detached-Eddy Simulation (DES) does not need to impose the interface between the statistical and LES regions. This is provided inherently by the choice of the turbulence length scale to use in the transport equations [14]. In order to avoid approaching the near-wall region by the LES zone, the Detached-Eddy Simulation has been improved in respect of the turbulence length scale, ensuring a quite significant statistical zone around the body, in the context of the Delayed Detached-Eddy Simulation (DDES) [15]. Moreover, improvement of the near wall modelling has been achieved by means of a suitable Wall-Modelled LES (WMLES) in order to allow the flow physics modelling in the very near wall region covering the viscous sublayer by means of finer grids (but more economic than the LES) in the context of the Improved Delayed Detached-Eddy Simulation (IDDES) [16]. Regarding the transonic buffet simulations, Deck [6] has used a successful zonal DES approach, using mostly statistical modelling in the outer regions far from the body. He provided a detailed prediction of the transonic buffet around the supercritical aerofoil OAT15A. Regarding the same configuration, Grossi et al. [7] performed a Delayed Detached-Eddy Simulation in the context of the ATAAC (Advanced Turbulence Simulations for Aerodynamic Application Challenges) European programme. This study succeeded in the prediction of the shock-wave self-sustained motion near the critical angle of incidence for the appearance of buffet, based on experimental results by Jacquin et al. [3,8]. Moreover, Szubert et al. [5] provided a detailed analysis of the buffet dynamics by means of the Organised Eddy Simulation (OES) approach, resolving the organised coherent modes and modelling the random turbulence background and using upscale turbulence modelling through stochastic forcing in order to keep the turbulent–non-turbulent shear-layer interfaces thin. In the present paper, the transonic buffet is applied on the V2C aerofoil within the TFAST program, at 7.0°, the maximum angle of attack allowed by the design, upstream Mach number 0.70 and Reynolds number 3.245×10^6. The fully turbulent case is studied by different URANS and DDES modelling in two and three dimensions respectively. The predictive capabilities of statistical and hybrid turbulence modelling approaches are discussed. A 2D study is first carried out to investigate the main flow characteristics in respect of the angle of attack as well as the influence of the transition location. The transition location effects are also studied in the buffeting regime, by imposing the laminarity at several positions. Based on these results, the main objective of the present article is to put ahead a coupling of the aforementioned CFD methods with a non-classical optimisation approach of the transition location in the steady and unsteady transonic regimes in respect of the drag reduction and lift-to-drag ratio maximisation.

2. Numerical method and turbulence modelling

2.1. Flow configuration

Concerning the design of the V2C wing, it was validated numerically by Dassault on a 0.25 m-chord length (c) profile by means of RANS computations for various angles of attack at freestream Mach numbers of 0.70 and 0.75, yielding chord-based Reynolds numbers of approximately 3.245×10^6 and 3.378×10^6 respectively. The study was performed using a compressible Navier–Stokes code adopting a two-layer $k - \varepsilon$ model, with the transition location being determined from the fully-turbulent flowfield using a three-dimensional compressible boundary-layer code by means of the N-factor amplification with a parabola method. The technique employed for laminarity and an initial design in respect of the transition prediction was based on the e^N method (Ref. [17] for instance). The aerofoil surface was generated in such a way that the N-factor remains small for low-to-moderate turbulence intensity levels, similar to the wind tunnel turbulence levels used for the present test-case for the experimental study currently in progress in the TFAST project. At Mach number 0.70, the flow separated between $\alpha = 6°$ and 7°. The amplification factor N was shown to be smaller than 3 up to the shock wave, thus guaranteeing laminar flow. At Mach number 0.75, the value of N remained smaller than 2 up to $\alpha = 7°$. For this Mach number, there was not buffeting phenomenon, whatever the angle of attack. Moreover, for incidences higher than 1°, the shock induces a separation of the boundary layer up to the trailing edge.

2.2. Numerical method

The simulations of the V2C configuration at upstream Mach number $M = 0.70$ and Reynolds number $\mathrm{Re} = 3.245 \times 10^6$ have been carried out with the Navier–Stokes Multi-Block (NSMB) solver. The NSMB solver is the fruit of a European consortium that included Airbus from the beginning of 90s, as well as main European aeronautics research institutes like KTH, EPFL, IMFT, ICUBE, CERFACS, Karlsruhe Institute of Technology, ETH—Swiss Federal Institute of Technology in Zurich, among others. This consortium is coordinated by CFS Engineering in Lausanne, Switzerland. NSMB solves the compressible Navier–Stokes equations using a finite volume formulation on multi-block structured grids. It includes a variety of efficient high-order numerical schemes and turbulence modelling closures in the context of URANS, LES and hybrid turbulence modelling. NSMB includes efficient fluid–structure coupling for moving and deformable structures. For the present study, the third-order of accuracy Roe upwind scheme [18] associated with the MUSCL flux limiter scheme of van Leer [19] is used for the spatial discretisation of the convective fluxes. A similar upwind scheme (AUSM) was used by Deck [6]. For the diffusion terms, second-order central differencing has been used. The temporal discretisation has been done by means of dual-time stepping and of second order accuracy. A physical time step of 5 μs has been adopted for 2D simulations. For the 3D simulations, the time step has been reduced to 0.1 μs after detailed numerical tests. A typical number of inner iterations of 30 was necessary for the convergence requirements in each time step.

The 2D grid has a C–H topology, and is of size 163,584 cells. The downstream distance of the computational domain is located at a mean distance of 80 chords from the obstacle. A grid refinement study has been carried out, by means of steady-state computations and using local time stepping, for the flow at $M_\infty = 0.70$ and $\alpha = 4.0°$ using the $k - \omega$ SST model [20] and assuming fully-turbulent boundary layer, with two other grids: one 50% coarser, and another 30% finer. Detailed results of this convergence study can be found in [7]. The grid retained for the present study gave

a maximum value of non-dimensional wall distance y^+ of about 0.55 with respect to the turbulence modelling. Fig. 1 shows the grid and the computational domain. For the 3D computations, the planar grid has been extruded to 59 cells uniformly distributed in the spanwise direction over a distance of $0.33 \times c$. The 3D grid contains about 9.65 M cells.

Boundary and initial conditions

On the solid wall, impermeability and no-slip conditions are employed. The far-field conditions are the characteristic variables extrapolated in time: the total pressure ($P_0 = 10^5$ Pa) and total temperature ($T_0 = 290$ K), as well as the upstream Reynolds number of 3.245 million and Mach number of 0.70. The upstream turbulence intensity is $Tu = 0.08\%$.
The initial conditions are those of a steady-state generated field in each case.

Turbulence modelling

In the context of URANS and hybrid turbulence modelling, the following models have been used respectively: the two-equation $k-\omega$ SST model of Menter [20] as well as the OES-$k-\varepsilon$ [5,21] and the DDES-$k-\omega$ SST models have been used with turbulence-sustaining ambient terms to prevent the free decay of the transported turbulence variables [22].

2.3. Optimisation method

In the context of the transition location study detailed in this paper, an optimisation of its location is proposed by employing a non-classical statistical learning approach. The principle consists in gathering a set of performance values, observed for different parameters, and constructing a statistical model (Gaussian Process) on this basis, that reflects the knowledge and uncertainties related to the performance function. Then, this model is employed to determine the most interesting simulations to carry out, in a statistical sense. This approach is repeated until convergence [23].

More precisely, the statistical model for the performance function f is constructed on the basis of a set of observed values $\mathbf{F_N} = \{f_1, f_2, \ldots, f_N\}$ at some points $\mathbf{X_N} = \{x_1, x_2, \ldots, x_N\} \in \mathbb{R}^d$ (here $d = 1$). $\mathbf{F_N}$ is assumed to be one realisation of a multivariate Gaussian Process which has a joint Gaussian distribution [24]:

$$p(\mathbf{F_N}|\mathbf{X_N}) = \frac{\exp\left(-\frac{1}{2}\mathbf{F_N}^\top C_N^{-1}\mathbf{F_N}\right)}{\sqrt{(2\pi)^N \det(C_N)}}, \tag{1}$$

for any collection of inputs $\mathbf{X_N}$. C_N is the $N \times N$ covariance matrix, whose elements C_{mn} give the correlation between the function values f_m and f_n obtained at points x_m and x_n. This is expressed in terms of a correlation function k, i.e., $C_{mn} = cov(f_m, f_n) = k(x_m, x_n; \Theta)$ with Θ a set of hyper-parameters, calibrated on the basis of known points (likelihood maximisation principle). The Matérn class of covariance stationary kernels, which gives a family of correlation functions of different smoothness [24], is used for k.

After calculations based on conditional probabilities, the probability density for the function value f_{N+1} at any new point x_{N+1} is:

$$p(f_{N+1}|\mathbf{X_N}, \mathbf{F_N}) \propto \exp\left[-\frac{(f_{N+1} - \hat{f}_{N+1})^2}{2\hat{\sigma}^2_{f_{N+1}}}\right], \tag{2}$$

where

$$\hat{f}_{N+1} = \mathbf{k_{N+1}}^\top C_N^{-1}\mathbf{F_N}, \tag{3}$$

$$\hat{\sigma}^2_{f_{N+1}} = \kappa - \mathbf{k_{N+1}}^\top C_N^{-1}\mathbf{k_{N+1}}, \tag{4}$$

with $\kappa = k(x_{N+1}, x_{N+1}; \Theta)$ and $\mathbf{k_{N+1}} = [k(x_1, x_{N+1}; \Theta), \ldots, k(x_N, x_{N+1}; \Theta)]^\top$. Thus, the probability density for the function value at the new point x_{N+1} is also Gaussian with mean $\hat{f}_{N+1}$ and standard deviation $\hat{\sigma}_{f_{N+1}}$. Therefore, the most likely value at the new point x_{N+1} is $\hat{f}_{N+1}$. This value will be considered as the prediction of the Gaussian Process model. The variance $\hat{\sigma}^2_{f_{N+1}}$ can be interpreted as a measure of uncertainty in the value prediction. If the evaluation is known to be noisy, the model can account for the observation noise by modifying the diagonal terms of the covariance matrix, on the basis of the noise variance estimated for each database point [25].

At each step of the optimisation procedure, this Gaussian Process model is exploited to determine new points to be simulated. The most popular strategy is the maximisation of the Expected Improvement (EI) criterion [23]. The maximisation of this criterion is numerically reached, by solving an internal optimisation problem using an evolution strategy.

3. Results

3.1. Two-dimensional study: angle of attack effects

This study has been carried out in URANS with the two-equation $k-\omega$ SST turbulence model [20] for an upstream Mach number $M_\infty = 0.70$. The angle of attack has been varied from 1.0° up to 7.0°, which is the maximum angle of attack for which the boundary layer is supposed to remain laminar from the leading edge to the shock wave. Initially, the computations adopt local time stepping. If convergence is not reached (i.e., a relative reduction of 10^{-6} in the residual), time-accurate simulations with a time step of 5×10^{-6} s are then carried out. Near the critical angle regarding the buffet, the angle of attack has been varied by an increment of 0.5° in order to refine the critical buffet range.

Fig. 2 shows the averaged distributions of the pressure coefficient for the full range of incidences and skin-friction coefficient for the steady cases. For angles of attack up to 5.0°, the flow is steady and rear separation is always present. The shock wave can be distinguished at 2.0°. As the angle of attack is further increased, the shock initially moves downstream, then it goes upstream for $\alpha > 3°$. From $\alpha = 4.0°$, a separation bubble appears and develops. The size of the rear separation steadily increases with the angle of attack (Fig. 2(b)).

The buffet onset, characterised by an oscillating shock wave, has been detected from 5.5°. The main frequency increases with incidence in the range of 80–82 Hz. At 5.5°, the amplitude of the shock-wave motion is still small, resulting in a slight slope in the C_p curve.

A detailed comparison of the results obtained in the present study by the NSMB code has been carried out by using the Edge code, an unstructured compressible finite volume CFD code developed by the FOI since 1997 in collaboration with industrial and academic partners. The wall pressure distribution is plotted in Fig. 3 for angles of attack between 1.0° and 7.0°. This comparison showed small differences close to the critical angle, but the results were very similar at lower and higher angles of attack. This ensures the validity of the present simulations, in absence of finalised experimental results within the TFAST program.

3.2. Transition location effect

Two flow conditions have been selected for a numerical investigation of the transition location effect on the SWBLI, due to their interesting flow physics. First, the steady interaction arising at $\alpha = 4.0°$ is addressed, featuring a reasonably strong shock just below the critical angle of attack for buffet onset. The second flow condition is the fully-established buffet regime at $\alpha = 7.0°$, which presents a large shock-wave motion region.

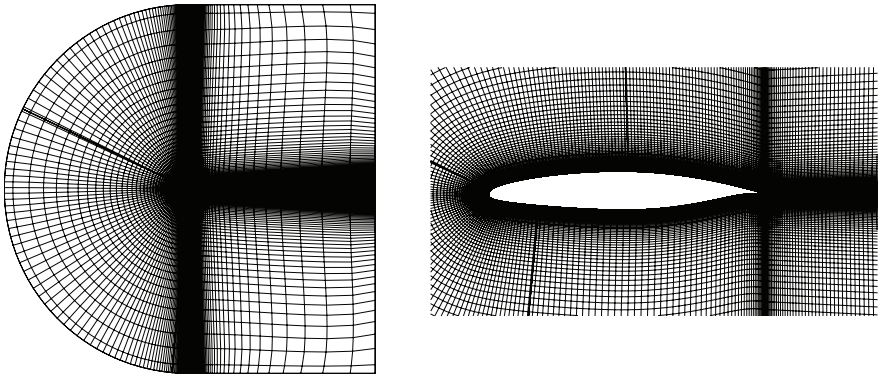

Fig. 1. Multiblock domain.

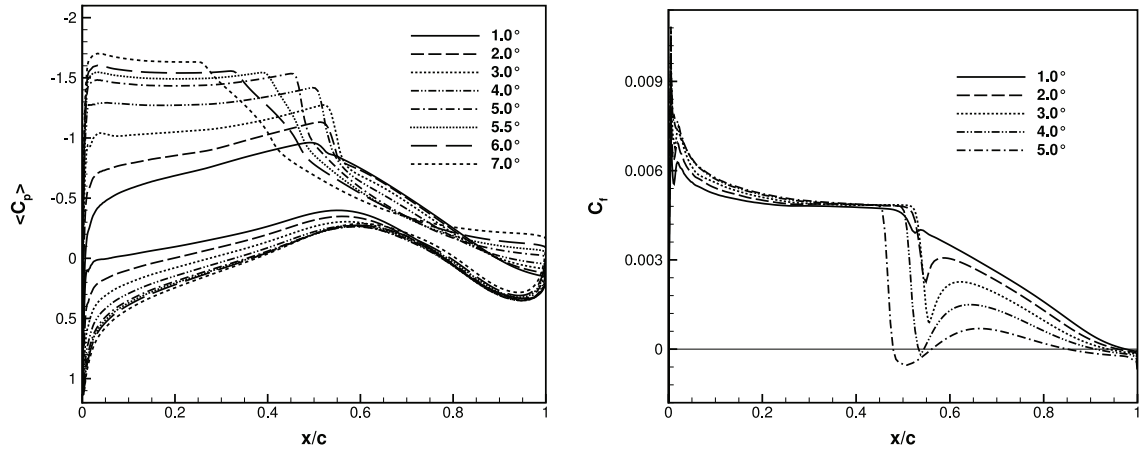

(a) Pressure coefficient. (b) Friction coefficient.

Fig. 2. Effect of the angle of attack on the steady and mean surface distributions and on the friction coefficient.

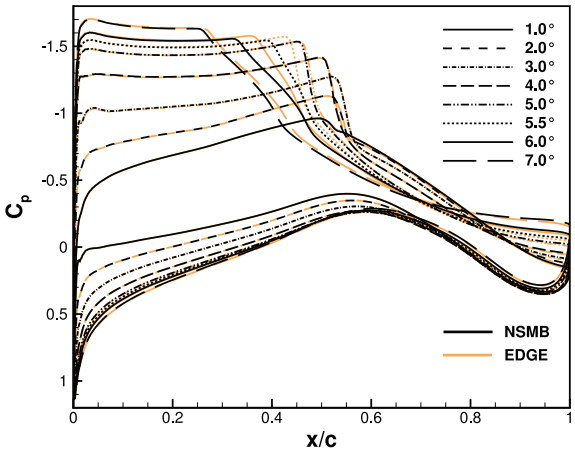

Fig. 3. Comparison of the mean wall pressure coefficient between NSMB end Edge codes, for angles of attack between 1.0° and 7.0°.

The transition is forced at the position x_t by imposing the turbulent viscosity $\nu_t = 0$ for $x < x_t$. Its location x_t is varied from the leading edge up to as close as possible to the shock wave. The influence of the tripping point over the selected steady and unsteady transonic flow-fields is presented in the following two subsections.

3.2.1. *Pre-buffet condition—Steady case*

Results presented in the previous sections showed that, at $\alpha = 4.0°$ and $M_\infty = 0.70$, the fully turbulent flow over the V2C aerofoil is near critical with respect to transonic buffet. At that incidence, the shock wave is strong enough to induce a small separation bubble and the adverse pressure gradient over the rear part of the aerofoil causes rear separation at about $x/c = 0.91$. The same flow condition has been recomputed considering different transition locations x_t from the leading edge up to the mid-chord, remaining steady in all cases. The pressure and friction coefficients distributions over the upper surface are plotted in Fig. 4 for some chosen values of x_t. The pressure coefficient indicates an increase of the suction effect as the transition position moves downstream, while the shock position moves downstream. These facts yield an increase of lift. The trailing-edge pressure decreases, as well as the C_p on both sides of the rear aerofoil part. The $x/C = 0.10$ case can be qualitatively compared with the case of the OAT15A aerofoil with fixed transition at $x/C = 0.07$, numerically studied by Grossi et al. [7] (Fig.9 in this reference) and compared with the experimental data of Jacquin et al. [8], where the same order of magnitude for the upstream and downstream pressure plateau is observed. A quite good comparison with the experiment is obtained. Therefore, despite the lack of experimental results up to now for the V2C aerofoil, a fairly good agreement can be expected between the present CFD and experiments under way in the TFAST project. Moreover, the DDES results of Grossi et al. [7] provide a higher trailing-edge suction than URANS, associated with more intense separation. This feature is a similar tendency to the DDES behaviour of the present study, discussed in Section 3.4, as well as with the zonal DES (ZDES) of Deck [6] (Fig. 6 in this reference). The effect of the transition location on the shock-wave position x_s, on the location x_b and length l_b of the separation bubble as well as on the rear separation position x_r are detailed in Table 1 for the complete set of simulations.

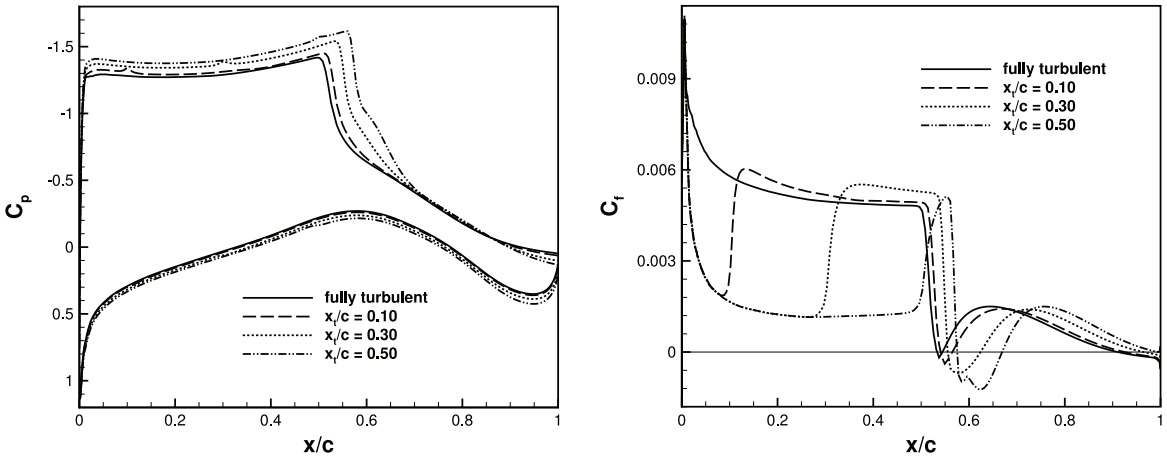

(a) Pressure coefficient.

(b) Friction coefficient.

Fig. 4. Steady surface distributions for selected transition locations at angle of attack of 4°.

Table 1
Transition location effect on the shock position, on separation and on the global aerodynamic coefficients.

x_t/c	Fully turb.	0.10	0.20	0.30	0.40	0.50
x_s/c	0.523	0.532	0.541	0.552	0.564	0.574
x_b/c	0.533	0.541	0.547	0.556	0.566	0.575
l_b/c (%)	1.1	2.4	4.7	6.8	8.5	9.4
x_r/c	0.911	0.925	0.946	0.965	0.981	–
C_L	0.8873	0.9174	0.9556	0.9919	1.029	1.061
$C_{D_f} \times 10^2$	0.610	0.574	0.510	0.460	0.396	0.334
$C_D \times 10^2$	2.080	2.069	2.102	2.171	2.268	2.365
L/D	42.7	44.3	45.5	45.7	45.4	44.9

Table 2
Transition location effect on the mean global coefficients, lift, drag and moment, for the unsteady.

x_t/c	Fully turb.	0.09	0.16	0.24
$\overline{C_D} \times 10^2$	6.163	6.501	6.604	6.715
$\sigma(C_D) \times 10^2$	0.9419	1.250	1.384	1.533
$\overline{C_L}$	0.9423	0.9718	0.9927	1.018
$\sigma(C_L)$	0.0854	0.1047	0.1132	0.1204
$\overline{C_m} \times 10^2$	−4.223	−4.932	−5.267	−5.676
$\overline{C_L}/\overline{C_D}$	15.3	14.9	15.0	15.2

The tripping points can be easily identified on the friction coefficient by the sudden and high increase in the wall shear when the boundary layer becomes turbulent. They can also be distinguished on the pressure coefficient in the form of slight pressure disturbances in the supersonic region. As the transition location is shifted downstream, which induced a reduction in the boundary layer displacement thickness, the shock wave moves downstream, which can be noted in Fig. 4, resulting in a stronger shock wave. As the laminar region increases, the progressively stronger shock wave makes the separation bubble grow continuously as indicated in Table 1 and by means of the C_f distribution. On the contrary, the rear separation gets smaller, yielding a larger pressure recovery and eventually vanishing for $x_t/c \approx 0.5$.

Table 1 provides also the force coefficients as the tripping point is varied. As the length of the laminar region, and thus the shock wave position move downstream, the lift increases due to a higher pressure difference between the upper and lower surfaces. The lift-to-drag ratio L/D is also provided. An optimal value is found near $x_t/c = 0.3$. However, this position of transition does not give the minimum value of the global drag coefficient, which is obtained for a transition located near $x_t/c = 0.10$, with a short laminar boundary layer region. This drag coefficient then increases with a longer laminar region, while the friction drag always diminishes as the laminar region becomes longer.

3.2.2. Unsteady regime

This study has been carried out to assess the influence of the transition point on the properties of the well-developed buffeting flow at 7.0°. Besides the fully-turbulent case, three tripping locations have been considered: $x_t/c = 0.09, 0.16$ and 0.24. For the latter, the most upstream position of the shock wave during buffet has been of about $x_t/c = 0.25$. This limits the displacement of the tripping point, because imposing $\nu_t = 0$ inside the shock-motion region would not be an acceptable approximation.

Fig. 5(a) presents the statistical pressure distributions obtained for each boundary layer tripping position. While the most upstream limit of the shock-motion range is not much sensitive to the transition location, its most downstream limit is strongly affected by the boundary layer state. As seen for the case $\alpha = 4.0°$, a larger extent of laminar boundary layer tends to move the shock wave further downstream by altering the displacement thickness distribution around the aerofoil. In fact, this effect can also be observed in the unsteady case regarding the mean shock-wave position, which roughly corresponds to the point of maximum pressure unsteadiness in Fig. 5(b). As the tripping point is placed downstream, the amplitude of shock motion becomes wider, increasing the fluctuation levels in the shock-wave region as well as the trailing edge unsteadiness. This can be observed in the series presented in Fig. 6, in terms of statistical pressure fluctuation fields. Comparing the fully-turbulent simulation with the case of the most downstream transition location ($x_t/c = 0.24$), the pressure unsteadiness increases by approximately 20% in the shock region and gets nearly two times larger near the trailing edge. The development of the shock-motion area as a function of the transition location is clearly visible in Fig. 6. In the last section of the article, an optimisation of the transition location effect has been carried out in respect of increasing aerodynamic performance.

Table 2 gives the average lift, drag and pitching moment coefficients for the three transition cases as well as for the fully-turbulent computation. The standard deviation σ of the aerodynamic forces is also presented. As for the steady flow at 4.0°, the values of the mean lift and of the moment magnitude increase as the triggering location moves towards the trailing edge. A slight augmentation in the mean drag is also noticed. As a result of the increasing shock-motion amplitude and of the overall flow unsteadiness, the standard deviations of the lift and drag coefficients also become larger as the extent of laminar boundary

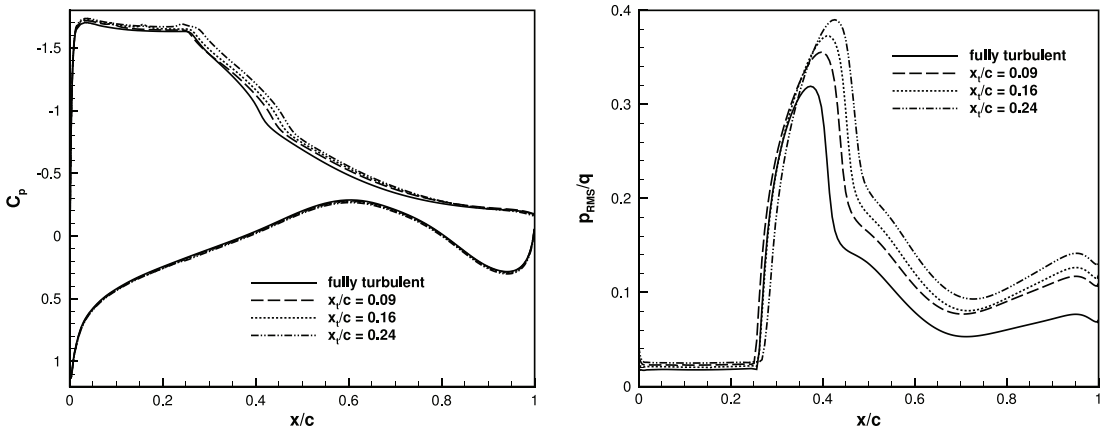

(a) Mean pressure coefficient.

(b) RMS value of pressure on the upper surface.

Fig. 5. Transition location effect on the statistical wall pressure at $\alpha = 7.0°$.

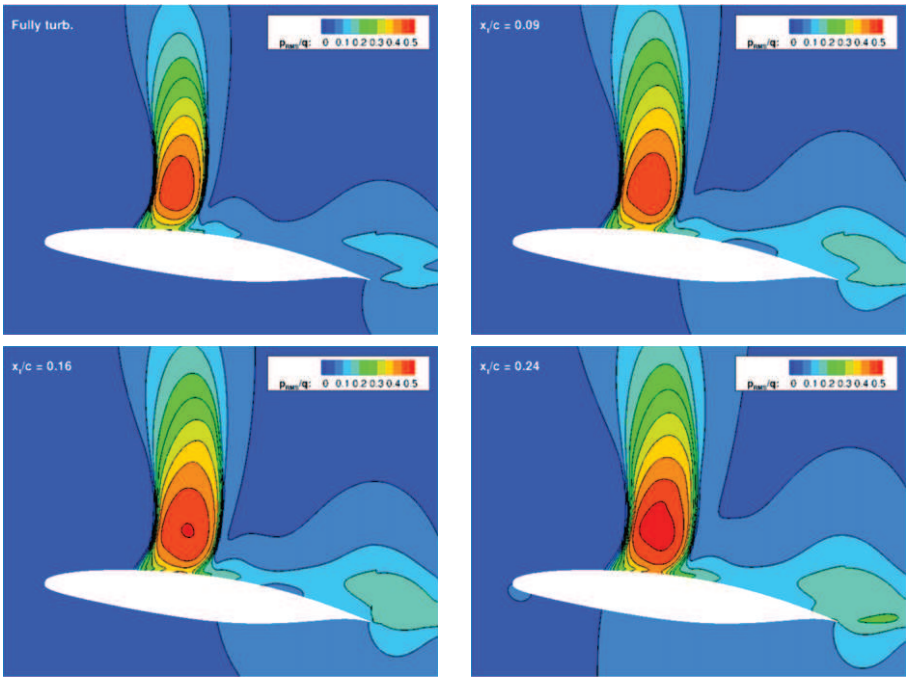

Fig. 6. RMS pressure fields for different transition locations at $\alpha = 7.0°$.

layer gets longer. Therefore the mean lift over mean drag ratio does not show much improvement whereas the laminar region is increased. Indeed, as the transition is located closer to the shock wave/boundary layer interaction, the boundary layer downstream detaches more easily than the fully-turbulent case, which gave here the higher lift-to-drag ratio. Moreover, due to the high angle of attack, the most upstream shock location is near 25% of the chord, which limits the flexibility on the transition position.

3.3. Optimisation of the tripping location

3.3.1. Problem description

As observed in the results above, the location of the transition point may have a significant impact on the aerofoil performance, in particular when unsteady boundary-layer/shock interactions occur. From designer point of view, it would be interesting to quantify this influence for the different cases (steady and unsteady) and determine the best tripping location, which maximises the aerofoil performance. In this perspective, a study is presented for the optimisation problem formulated as:

$$\text{Maximise} f(x) = \overline{C_L/C_D} \quad \text{for } x \in I, \tag{5}$$

where x is the stripping location and I the allowed search interval. This is a PDE-constrained optimisation problem including a single parameter. The major difficulty arises from the computational cost related to the unsteady flow simulations and the possible noisy prediction of the performance due to the presence of numerical errors (discretisation, time integration). The use of a classical descent optimisation method is tedious, due to the unsteady functional gradient estimation. Alternatively, stochastic approaches like genetic algorithms or evolution strategies require too many evaluations to be practically tractable.

3.3.2. Results for the steady case

A steady flow problem is first considered, corresponding to the 2D case described above for an incidence $\alpha = 4.0°$. In this context, the performance is simply the lift-to-drag ratio computed

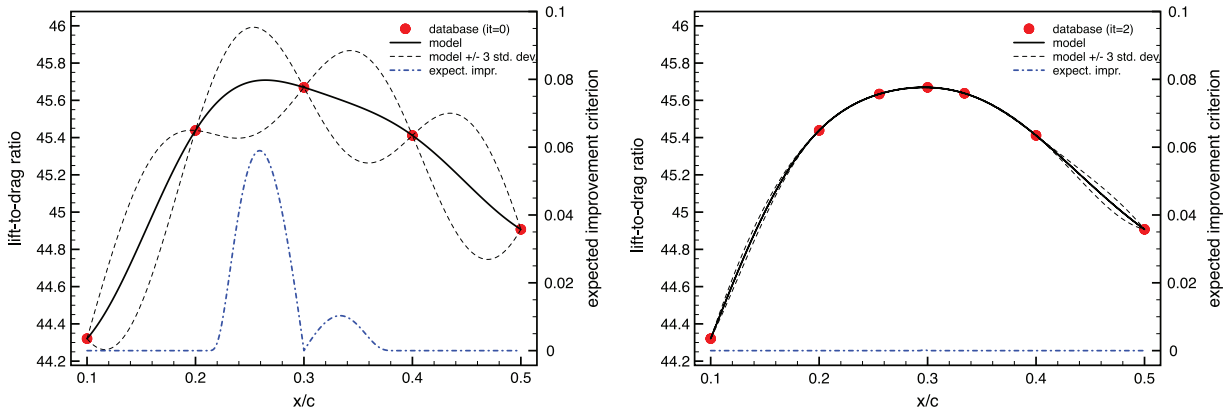

Fig. 7. Statistical model for the lift-to-drag ratio with regard to the tripping location (steady case), for iteration 0 (left) and iteration 2 (right).

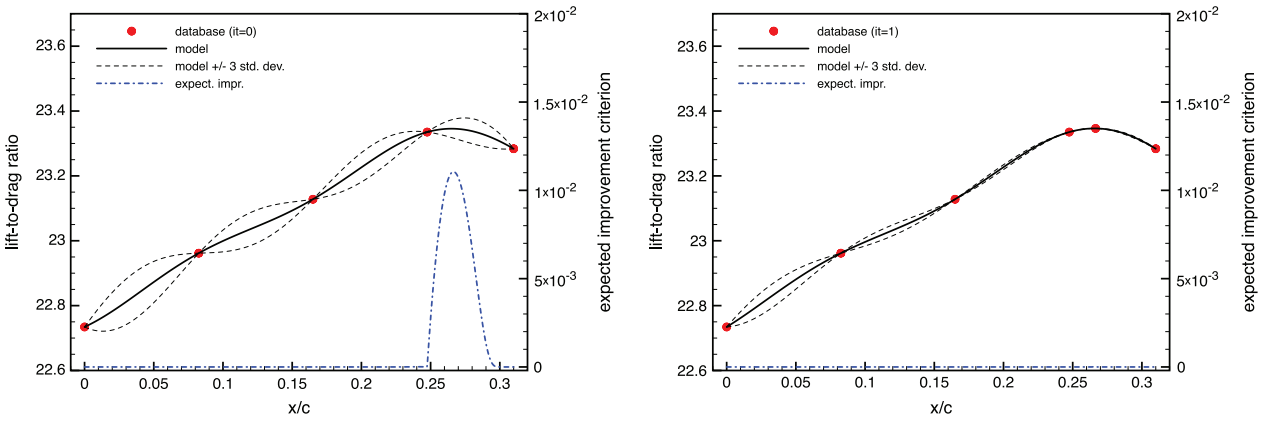

Fig. 8. Statistical model for the lift-to-drag ratio regarding the tripping location (unsteady case), for iteration 0 (left) and iteration 1 (right).

at convergence. The tripping location can vary in the interval $I = [0.1c, 0.5c]$. Five configurations, corresponding to $x_1 = 0.1c$, $x_2 = 0.2c$, $x_3 = 0.3c$, $x_4 = 0.4c$ and $x_5 = 0.5c$, are achieved independently to construct a first database. A Gaussian Process model for the lift-to-drag ratio function is then constructed according to the previous section and illustrated by Fig. 7. In this figure, one can see the model itself, its associated standard deviation and the expected improvement (EI) criterion used to drive the search and select the next point to simulate. As can be seen, after two additional simulations, the standard deviation is strongly reduced and the expected improvement almost zero. Moreover, the next point to simulate, as proposed by the EI criterion, is very close to a know point and the mesh accuracy for the tripping point location is reached. As consequence, the optimisation process is stopped. Finally, two conclusions can be drawn from this optimisation exercise: a large area, from $x = 0.25c$ to $x = 0.35c$ corresponds to a very high lift-to-drag ratio, and the best performance is obtained for a tripping location close to $x = 0.3c$.

3.3.3. Results for the unsteady case

We consider then the more challenging case corresponding to unsteady flows, for which shock-wave/boundary-layer interactions generate buffets. This study has been carried at an incidence of $\alpha = 5.8°$. In this case, the shock-motion amplitude is limited and allows for a wider range of transition locations than at higher incidence. Here, the performance function is the time-averaged lift-to-drag ratio, computed once a quasi-periodic flow is obtained. The admissible interval for the tripping point is moved upstream $I = [0, 0.31c]$, to avoid the shock to be located in the laminar area. Five configurations, corresponding to the fully turbulent case $x_1 = 0$, then $x_2 = 0.0825c, x_3 = 0.165c, x_4 = 0.2475c$ and $x_5 = 0.31c$, are achieved independently to construct a first database. Note that the configuration $x_5 = 0.31c$ exhibits instabilities after a long time integration. For this case, the time-averaging process has been shortened to avoid these phenomena.

Fig. 8 represents the Gaussian Process model for the time-averaged lift-to-drag ratio, at iterations 0 and 1. The initial model (iteration 0) yields an Expected Improvement criterion localised around a maximum at $x_6 = 0.2665c$. This configuration is simulated and added to the database, yielding an updated model (iteration 1). Since the lift-to-drag ratio computed by simulation is very close to the one predicted by the model, the variance of the model is strongly reduced, as well as the Expected Improvement criterion, as soon as the first iteration. Therefore, the optimum tripping value should be close to x_6.

To validate this result, three additional test points (TP) are simulated *a posteriori*, corresponding to $x_1^{TP} = 0.12c$, $x_2^{TP} = 0.2c$, $x_3^{TP} = 0.25c$ and the results are compared to the model prediction. It appears that the performance value for x_3^{TP} slightly differs from the model prediction, due to the fact that the unsteady flow exhibits some low frequency oscillations, which make the estimation of the time-averaged lift-to-drag ratio more difficult. To account for this uncertainty in the performance estimation, a variance estimate of the time-averaged lift-to-drag ratio is computed for all configurations, by using a classical moving average procedure. This variance is introduced into the Gaussian Process model as an observation noise. Fig. 9 shows the resulting model, that does not interpolate database points anymore, against additional test points. As can be observed, the uncertainty in the performance estimation is not negligible in this context, especially when the tripping point is close to the shock wave location, which corresponds to the best performance area (x

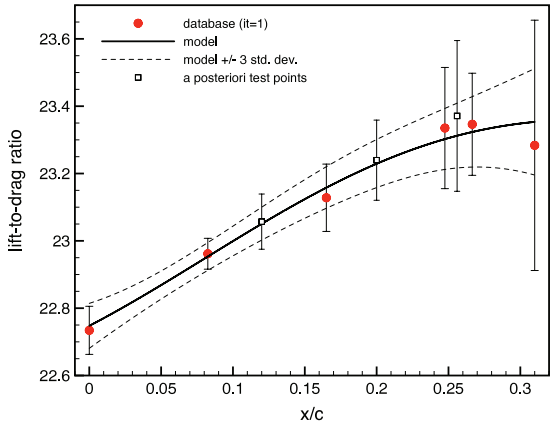

Fig. 9. Statistical model for the lift-to-drag ratio as a function of the tripping location (unsteady case), accounting for the observation variance.

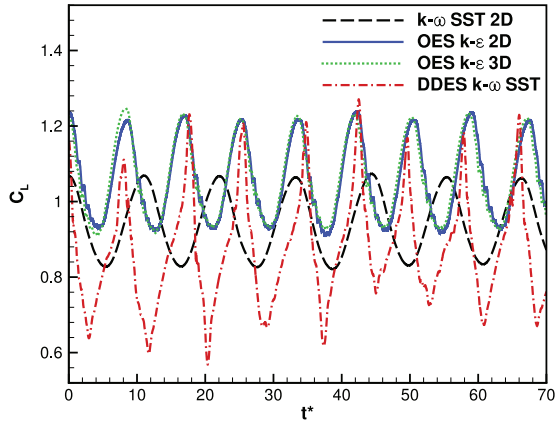

Fig. 10. Comparison of the time-dependent evolution of the lift coefficients between URANS $k-\omega$ SST, 2D and 3D OES-$k-\varepsilon$ and DDES-$k-\omega$ SST.

between $0.2c$ and $0.3c$). Nevertheless, the statistical model allows having a better analysis of the problem. In particular, one can underline that the confidence interval of the model is smaller than the standard deviation of the observations, in the zone where several points have been computed. In conclusion, for this unsteady case, the aerofoil performance is better for a tripping point x between $0.2c$ and $0.3c$, but the corresponding flows exhibit additional unsteadiness because of interaction with the existing buffet instability, that could be damageable in real conditions.

3.4. Three-dimensional simulation of the fully-turbulent case

The DDES-$k-\omega$ SST model has been applied, using the same numerical scheme as the 2D computations and time step $\Delta t = 10^{-7}$ s, in order to examine the 3D dynamics of the fully developed transonic buffet occurring over the V2C aerofoil at $M_\infty = 0.70$ and $\alpha = 7.0°$. The turbulence length scale provided by the RANS part is computed using local turbulence properties and is given by $\sqrt{k}/(\beta^*\omega)$. A comparison of the DDES results with the URANS $k-\omega$ SST [20] as well as the 2D and 3D OES-$k-\varepsilon$ [5,21] is provided. Concerning the grid spacing, which has to be nearly isotropic in the LES region, in respect of the DDES choice of the turbulence length scale, 59 cells have been distributed over a $0.33c$ spanwise length with a constant spacing, resulting in a final grid of about 9.65 M cells. The computations have been carried out in the SGI Altix supercomputer at CINES (Centre informatique national de l'enseignement supérieur), by using 1024 parallel processors in MPI.

3.4.1. Flowfield dynamics

The time-dependent lift coefficient according to the aforementioned models is presented in Fig. 10 for the fully established regimes, beyond transient phases. While in URANS $k-\omega$ SST the lift coefficient oscillates quasi-harmonically at a frequency of 82 Hz, the DDES produces sharp-like and much stronger lift fluctuations. The high slope of the curve indicates that the shock-motion speed is relatively high, especially during the lift fall when the flow separates and the shock moves upstream. The predicted buffet frequency in the DDES case is approximately 108 Hz. The large amplitude of the fluctuations suggests existence of modelled-stress depletion (MSD) [15] and indicates that shock-wave motion is wider than in case of the $k-\omega$ SST model. The OES-$k-\varepsilon$ model provides an almost sinusoidal behaviour of the oscillations at 107 Hz and a slightly higher amplitude than the $k-\omega$ SST. This behaviour is in-between the URANS and DDES evolutions. The spectral analysis of the lift coefficient is shown in Fig. 11, where $\mathrm{St} = f\,U_0/c$ is the non-dimensionalised frequency, with f the frequency in Hz,

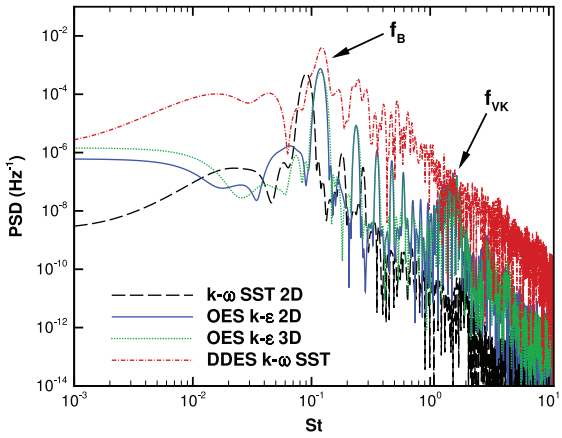

Fig. 11. Comparison of the power spectra density of the lift coefficients time-dependent evolution between URANS $k-\omega$ SST, 2D and 3D OES-$k-\varepsilon$ and DDES-$k-\omega$ SST.

$U_0 = 228$ m s^{-1} the freestream velocity and $c = 0.25$ the chord of the aerofoil. These spectra are similar to the experiments by Jacquin et al. [8,3] concerning the buffet mode identification for the OAT15A supercritical aerofoil configuration in the same Mach and Reynolds number range. Moreover, the OES modelling sensitised to reduce the turbulent diffusion and enhance coherent structure appearance, provides spectra of a similar shape to the study of Szubert et al. [5] carried out for the OAT15A, showing the buffet frequency as well as a spectral bump related to the von Kármán mode associated with alternating vortices past the trailing edge, as shown in Fig. 17 for the V2C profile. This two-mode interaction sustains a feedback loop including also Kutta waves as shown in this figure, in qualitative comparison with experiments (Fig. 18). This aero-acoustic feedback mechanism was schematically presented in Lee [26].

Table 3 shows the values of the buffet frequency as well as the corresponding Strouhal numbers and mean and RMS values of lift coefficient per turbulence model.

In the spectra, the DDES-$k-\omega$ SST provides the highest continuous spectral level, indicating a lower turbulence diffusion rate predicted by this model (also shown in the turbulent viscosity field as discussed at the end of this section, Fig. 20). The $k-\omega$ SST and OES-$k-\varepsilon$ provide in addition to the main frequency bump corresponding to the buffet instability, bumps beyond 2000 Hz, which are related to the von Kármán instability and other vortex interactions past the trailing edge as discussed in [5]. In all the spectra, the presence of the buffet mode is illustrated by a

Table 3
Comparison of the aerodynamic coefficients and buffet frequency between turbulence modelling methods for 9 periods of buffeting.

Turb. model.	$k-\omega$ SST	OES-$k-\varepsilon$ 2D	OES-$k-\varepsilon$ 3D	DDES-$k-\omega$ SST
$\overline{C_D} \times 10^2$	6.163	8.119	8.188	9.106
$\overline{C_L}$	0.942	1.059	1.061	0.875
$\sigma(C_L)$	0.084	0.106	0.106	0.145
RMS(C_L)	0.946	1.067	1.067	0.886
f_B (Hz)	82	107	108	108
St $= f_B\, c/U_0$	0.09	0.118	0.12	0.12

frequency bump instead of a sharp peak, because of the non-linear interactions of the buffet mode with the von Kármán, shear-layer and other more random motions downstream. Therefore, the present simulations capture the dynamics of the buffet and near trailing-edge instability modes and of their interaction producing a multitude of frequencies between these modes, which sustain a feedback loop among the shock oscillation region, the separated shear layer and the near wake. These interactions and feedback loop, schematically reported in [26], have been analysed in detail by [5], using time–frequency analysis by means of wavelets and Proper Orthogonal Decomposition in addition to a spectral analysis. Fig. 12 shows the mean surface pressure coefficient. All models are in agreement in the suction side, with a slight increase of lift near the trailing edge in case of OES-$k-\varepsilon$, which corresponds to a higher averaged lift coefficient (Table 3). The $k-\omega$ SST model produces the shortest inclination of the C_p within the shock region and therefore the less developed shock oscillation amplitudes. The largest amplitudes correspond to the DDES-$k-\omega$ SST, as can be implied by the high amplitude lift coefficient oscillations. This feature, accompanied by a higher trailing-edge pressure plateau, is similar to a thicker aerofoil's C_p, as for example in the experimental study of McDevitt et al. [1] for a circular-arc aerofoil in transonic regime, as well as in the ZDES of Deck [6] (Fig. 6 in this reference) and in the DDES-Spalart–Allmaras study of Grossi et al. [7] (Fig. 9 of this reference). This common tendency occurs among these approaches using different numerical schemes (the AUSM in Deck's study, the 3rd order Roe upwind scheme in Grossi's study as well as in the current study). Therefore, it seems that the hybrid RANS–LES models provide a higher level of suction and flow detachment in the present family of supercritical aerofoils. This behaviour can be explained by means of turbulent viscosity levels of the three modelling approaches used in the present study and by considering the frontier between the URANS and LES regions, commented in a dedicated discussion at the end of this section. The OES-$k-\varepsilon$ produces an in-between behaviour, similar to the flow simulations around the supercritical OAT15A aerofoil with fixed transition at 7% (Szubert et al. [5]) which compare quite well to experimental results by Jacquin et al. [8,3]. Therefore, it can be reasonably supposed that in the V2C case, a fairly good comparison of the present URANS studies (better than the DDES behaviour) is expected from the ongoing experimental campaign in the TFAST project.

Fig. 13 shows the mean pressure fields superimposed with streamlines according to the previous models. The DDES illustrates the largest separation area and the OES indicates a higher circulation intensity, corresponding to the lift increase. The $k-\omega$ SST and OES-$k-\varepsilon$ provide qualitatively comparable recirculation regions. The same feature stands for the mean velocity profiles shown in Fig. 14, in the near-wall region concerning the locations $x/c = 0.2$, 0.4, 0.6 and 0.8. In the intermediate region at $x/c = 0.4$, the $k-\omega$ SST shows a narrower boundary-layer thickness. The DDES illustrates the wider shock motion, yielding to a less expanded velocity profile at $x/c = 0.2$ and a much more separated one at $x/c = 0.8$ than the other two models.

A series of flow snapshots is presented in Fig. 15 for one period of buffet in the case of the DDES-$k-\omega$ SST. It

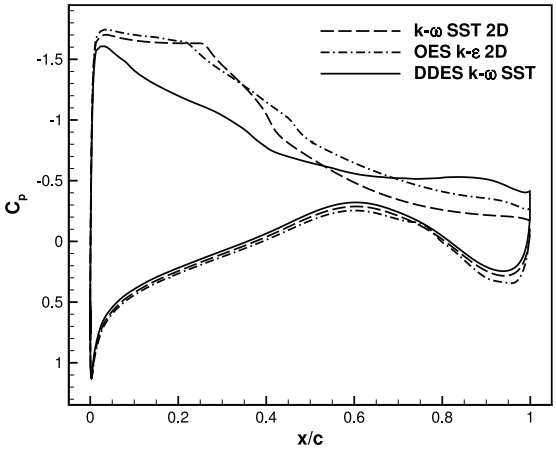

Fig. 12. Comparison of the wall pressure coefficient between URANS $k-\omega$ SST, OES-$k-\varepsilon$ and DDES-$k-\omega$ SST.

helps understanding the dynamics of the flow predicted. The figures illustrate instantaneous isosurfaces of non-dimensional Q-criterion for $Q(c/U)^2 = 75$ as a function of the non-dimensional time $t^* = tU/c$, where $t^* = 0$ is an instant of maximum lift. Surfaces are coloured with the Mach number. During the upstream travel of the shock (Fig. 15(a)), alternate vortex shedding can be observed at the trailing edge. The primary structures are always three-dimensional. As the shock approaches the leading edge, the flow over the upper surface gets fully separated and the shear layer becomes unstable (Fig. 15(b)). Such intense separation generates a large wake combining the eddies produced in the shear layer and the trailing edge structures. As the shock and the separation point move downstream, the height and streamwise extension of the separation region decrease and the amount of resolved flow structures reduces as seen in the sequence in Fig. 15(c). Unlike in URANS, a considerable amount of separation always exists on the rear part of the aerofoil. While the shear layer becomes stable as the shock wave approaches its most downstream position, the alternate vortex shedding at the trailing edge is always present during buffet (Fig. 15(d)).

A series of mid-span plane snapshots is presented in Fig. 16 and in Fig. 17 for one period of buffet regarding the DDES-$k-\omega$ SST and the OES-$k-\varepsilon$ respectively. These instantaneous fields are similar to Schlieren visualisations and illustrate the shock motion, the Kutta waves travelling from the trailing edge to upstream positions, the von Kármán vortices past the trailing edge and the smaller-scale Kelvin–Helmholtz vortices in the separated shear layers, among other more chaotic vortex structures. The DDES-$k-\omega$ SST simulations provide a quite rich turbulence content and a large shock motion and separation regions, extended near the leading edge. The OES-$k-\varepsilon$ provides a shorter shock-motion amplitude and a visualisation of the compressibility effects in qualitative agreement with D.W. Holder [27], Fig. 18.

In order to understand the DDES behaviour which provided such a large separation, the distribution of the RANS and LES regions has been monitored allowing assessment of the present

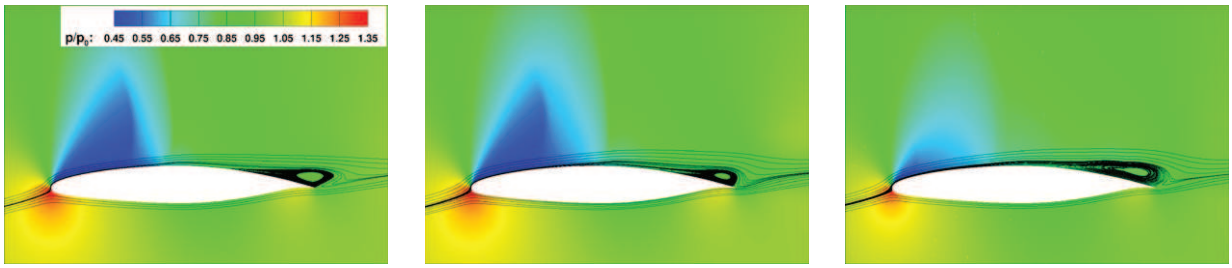

(a) URANS $k-\omega$ SST. (b) OES-$k-\varepsilon$. (c) DDES-$k-\omega$ SST.

Fig. 13. Mean pressure fields and streamlines around the profile.

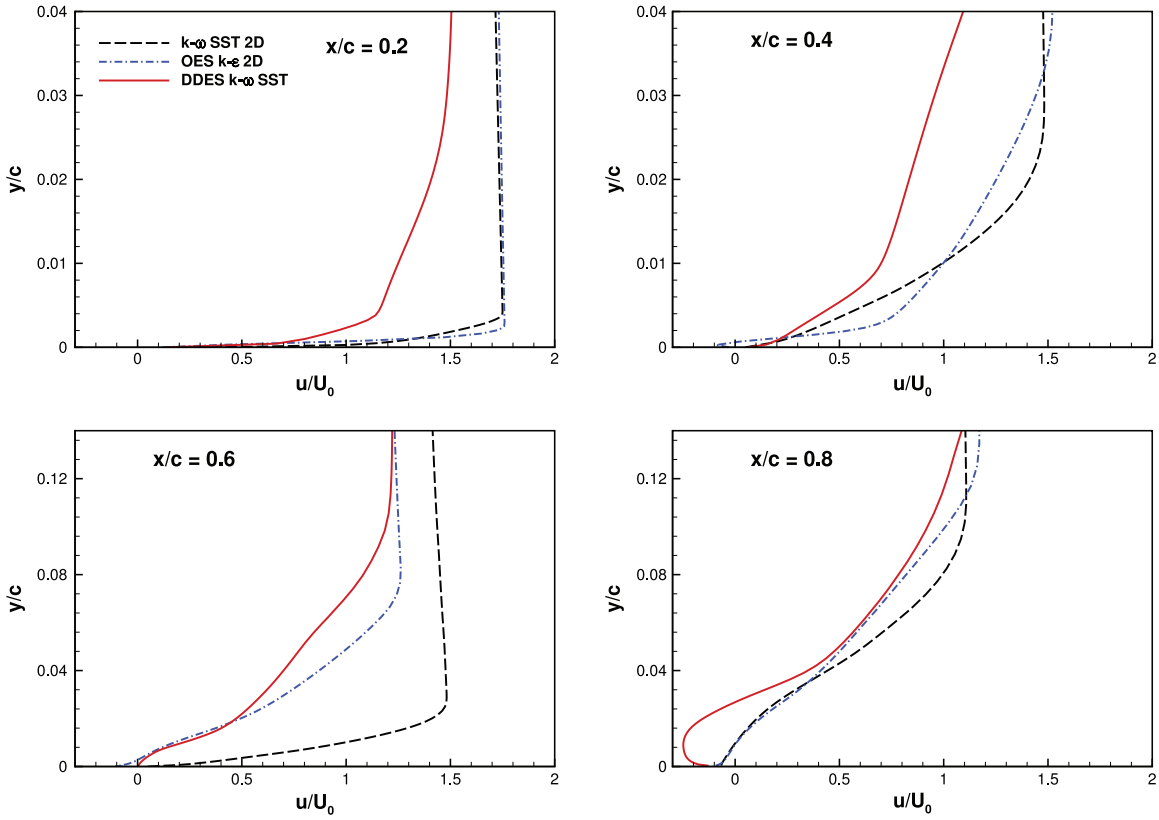

Fig. 14. Mean velocity profiles at locations $x_t/c = 0.2$, 0.4, 0.6 and 0.8 for URANS $k-\omega$ SST, OES-$k-\varepsilon$ and DDES-$k-\omega$ SST.

DDES ability to switch between the two modes (URANS and LES) during buffet and of the size of the two regions. The instantaneous distributions of the delaying function $1-f_d$ of the DDES at four phases of buffet are given in Fig. 19. The irregular black areas over the upper surface indicate large regions of separation, even when the shock is at its most downstream position (Fig. 19(d)), where a large amount of rear separation exists on the upper surface. This analysis shows the existence of a RANS-mode layer covering the near-wall region around the V2C aerofoil. The overall height of this layer seems to be relatively small. This might cause some degree of MSD [15] due to the erroneous penetration of the LES mode into attached boundary layers, which facilitates separation. This behaviour was also observed in the DDES studies by Deck [29] improved by a zonal DES approach. In this article, Fig. 19, the development of the shear layer instabilities appear at a considerable distance past the separation point, whereas in our case they appear earlier (Fig. 15). The article also by Uzun et al. [30] has been referenced thanks to a clear representation of the f_d function delimiting the RANS region in the boundary layer around the body (Fig. 7 in their study), which is similar to the behaviour of this function in the present study and the fact that the shear layers past the cylinder are treated by LES in that study. In addition, these shear layers (Fig. 8 in that paper) display the instability development at a considerable distance downstream of the separation point in respect of the appearance of Kelvin–Helmholtz vortices. The same behaviour was reported by Mockett et al. [31] concerning the acceleration of the transition between RANS and LES in a free shear layer by various DES approaches. The present DDES behaviour illustrated by the previous flow visualisations, the mean C_p and lift coefficients can be explained as follows: the pressure near the trailing edge (Fig. 12) is underestimated in the case of DDES, displaying a significant suction comparing with the URANS cases. The DDES provides a higher shock's excursion from the leading edge up to more than half of the chord yielding a pressure increase in this area. Therefore, the resulting lift is lower than in URANS and consequently, the corresponding circulation is lower.

In this case, the pressure aspiration effect on the suction side and the overall separated region seems to be more intense than in other cases. The related instabilities are more pronounced and start more upstream in the shear layers than in cases where the excursion of the shock has a shorter amplitude. These results are

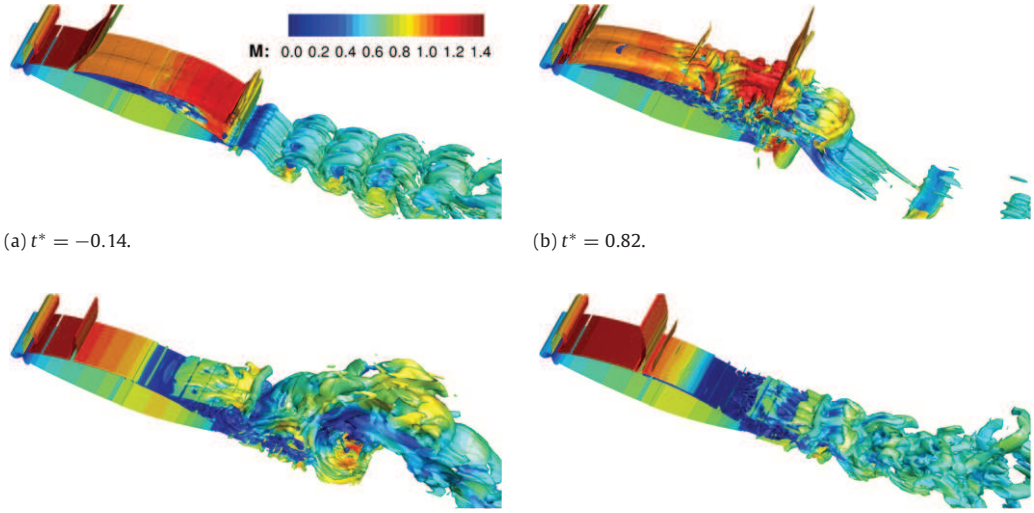

(a) $t^* = -0.14$. (b) $t^* = 0.82$.

(c) $t^* = 3.28$. (d) $t^* = 4.92$.

Fig. 15. Instantaneous Q-criterion isosurfaces for $Q(c/U)^2 = 75$. (For interpretation of the references to colour in this figure legend, the reader is referred to the web version of this article.)

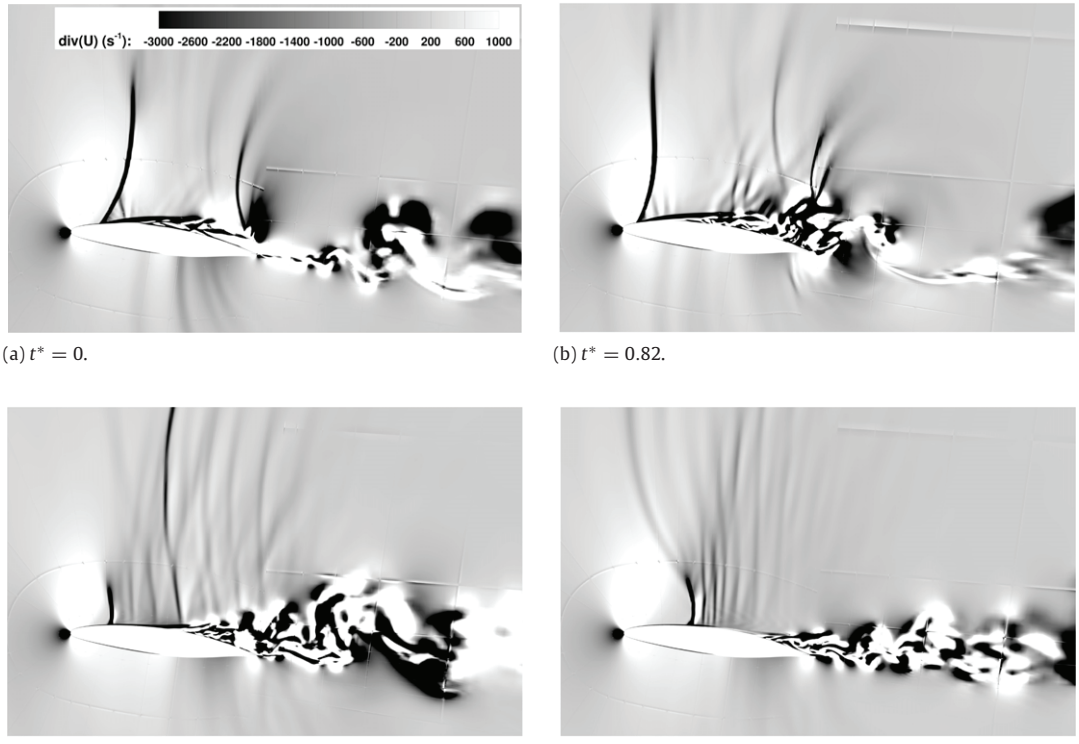

(a) $t^* = 0$. (b) $t^* = 0.82$.

(c) $t^* = 3.28$. (d) $t^* = 4.92$.

Fig. 16. Divergence of velocity field—DDES-$k-\omega$ SST.

not linked to a strong delay in the formation of instabilities in the shear layer and in the overall suction region but on a too early onset of instabilities. This is viewed in the 3D plots of Fig. 15 where a strong and rich statistical content of vortices is developed in the suction area from practically the leading edge. Indeed, the difference between the "peaky" shape and the more "sinusoidal" one indicates that at the same instant, the lift is lower in the DDES case, upstream and downstream of the sharp peak. This behaviour is in accordance with the "peaky" shape of the lift coefficient displayed by the DDES-SST, comparing to the OES simulations (Fig. 10). This is in accordance with the aforementioned elements concerning the pressure distribution and the mean lift. The reasons for this can be as follows. In Fig. 19, the frontier between RANS and LES regions are shown. It can be seen that a significant part of the shear layer is handled by RANS computation (see dark zone past the separation point), but this does not inhibit the development of instabilities which are quite displayed in the upstream region. Moreover, the dark region surrounding the aerofoil near the wall is associated with RANS computation within the boundary layer. Therefore, the LES approaches drastically the wall region. This would need a finer grid in this area. Moreover, the reason for the DDES behaviour, also depicted by another partner (URMLS) within the TFAST European program (M. Bernardini, S. Pirozzoli, private communication), by using DDES-SA and a different numerical code, may be due to the turbulent viscosity produced by the model in association with the grid. In order to illustrate the effect of

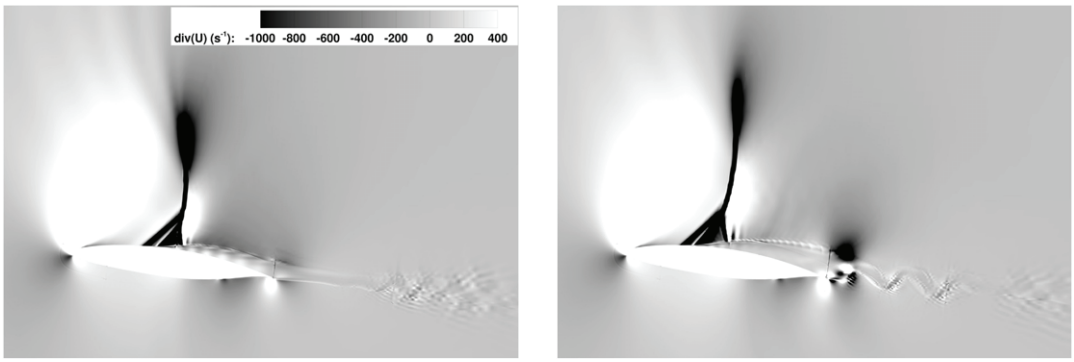

(a) $t^* = 0$. (b) $t^* = 0.83$.

(c) $t^* = 3.28$. (d) $t^* = 4.92$.

Fig. 17. Divergence of velocity field—OES-$k - \varepsilon$.

the turbulent viscosity produced by the turbulence model, the ratio ν_t/ν is plotted in Fig. 20. It can be seen that the DDES produces a much lower turbulence viscosity (order of 200 in the separated regions) than the URANS-OES (order of 1800), leading to a lower dissipation level which excessively amplifies smaller-scale structures in the separated area and a more intense separation. In the OES case, the higher ν_t level improves this feature. The use of the Spalart–Allmaras model instead of the $k - \omega$ SST in the DDES provided even higher shock amplitude oscillations because the maximum ratio ν_t/ν was of order 250 [32], Fig. 6.15 in this reference. This behaviour was shown for the lift oscillation in [33, Fig. 13]. As can be shown in the lift oscillations, the 'peaky' behaviour disappears on the benefit of a more sinusoidal shape with a higher pressure plateau up to 30% of the chord, a shorter excursion of the shock as well as an improved effect on the pressure 'plateau' near the trailing edge with less suction (see Fig. 12).

In a study in progress, the OES-$k - \varepsilon$ model results will be analysed in detail, in order to take benefit from the more regular buffet oscillations and simultaneously from the formation of the additional frequency bumps shown in Fig. 11, as in the study by Szubert et al. [5].

4. Conclusion

The present study analysed the SWBLI in the case of the transonic flow around the V2C-Dassault Aviation profile in two and three dimensions by means of statistical and hybrid RANS–LES turbulence modelling in the high Reynolds number regime of 3.245 million. The critical range of angle of attack for the buffet appearance has been investigated by means of 2D URANS computations and found near 5.5°. The different flow phenomena occurring around the aerofoil for various angles of attack at Mach number 0.70 have been analysed. The pressure and skin friction distributions have shown the angle of attack effect on the shock

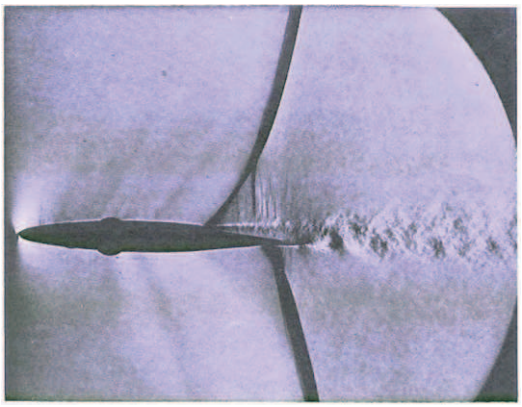

Fig. 18. Schlieren photograph of the eddying wake following a shock-induced flow separation.
Source: Courtesy of National Physical Laboratory, England; study by Duncan et al. [28]; photo by D.W. Holder.

wave position, as well as on the state of the boundary layer interaction with the shock foot. The influence of a fixed transition location on the flow physics has been studied in the steady and unsteady cases and particularly on the buffet dynamics. Based on these results, a major outcome is a non-classical optimisation procedure coupling the CFD results with a Kriging method, applied to the transition location regarding the averaged aerodynamic coefficients. In the steady case, an optimal position of the fixed transition has been found near $x_t/c = 0.30$ regarding the averaged lift/drag ratio. Particularly, the transition location effect on the unsteady case with buffeting conditions (angle of attack of 5.8°) has been analysed with the same method and yields an optimum position at $x_t/c = 0.2665$. These elements contribute to the improvement of laminar wing design for future generation of

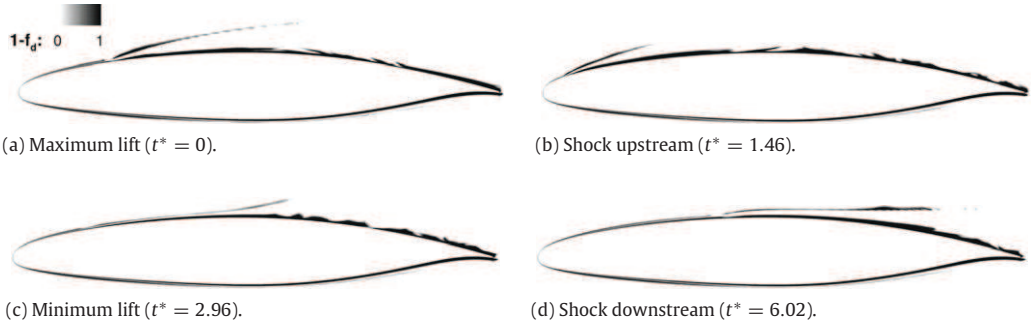

(a) Maximum lift ($t^* = 0$). (b) Shock upstream ($t^* = 1.46$).

(c) Minimum lift ($t^* = 2.96$). (d) Shock downstream ($t^* = 6.02$).

Fig. 19. RANS and LES regions around the V2C aerofoil according to the DDES-$k - \omega$ SST.

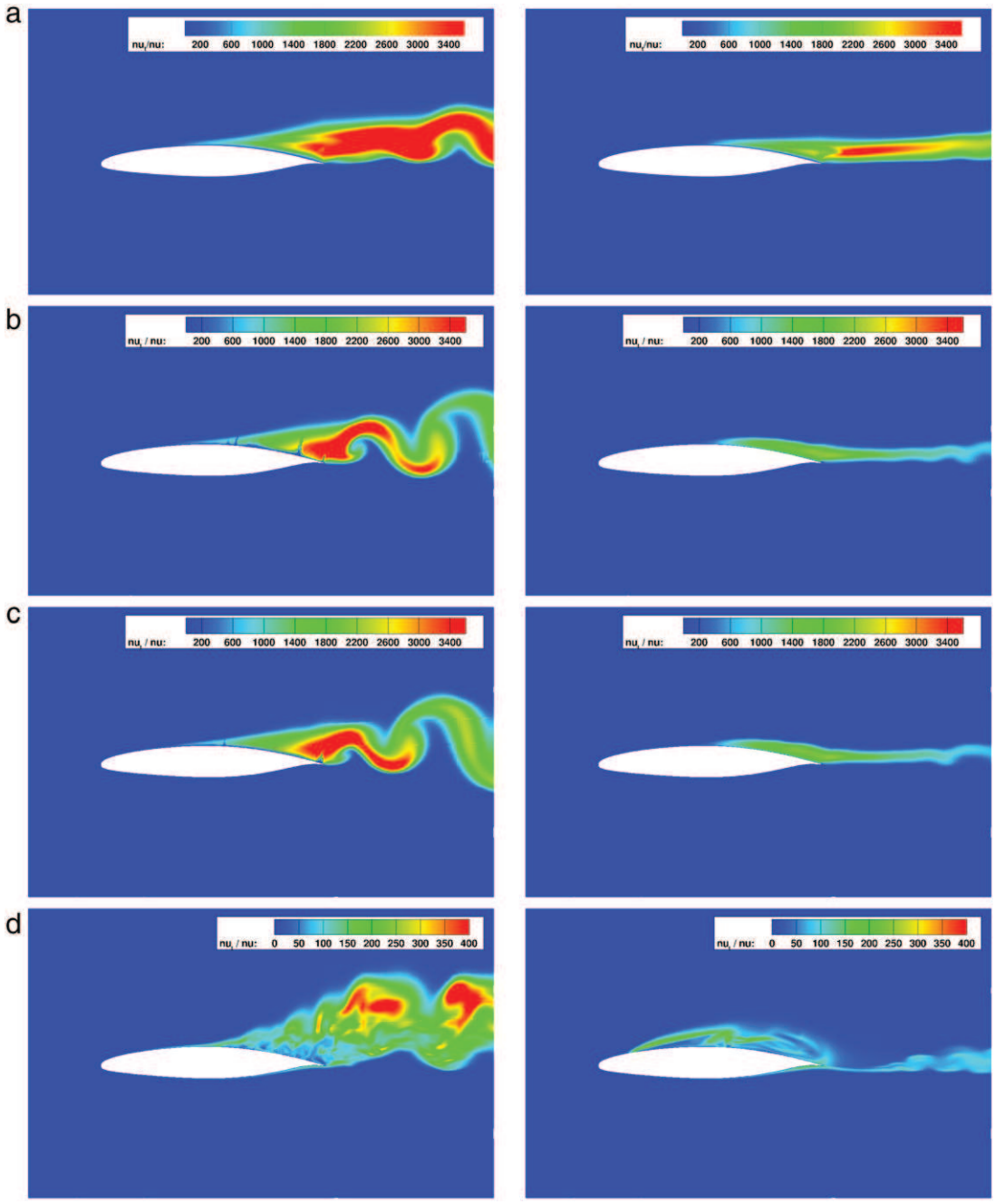

Fig. 20. Comparison of the turbulence viscosity field between URANS $k - \omega$ SST (a), 2D (b) and 3D (c) OES-$k - \varepsilon$ and DDES-$k - \omega$ SST (d) at minimum (left) and maximum (right) lift.

aircraft's wings, in respect of the greening requirements of the *Horizon 2020* objectives. Furthermore, the flow dynamics of a fully developed buffet case at angle of incidence of 7.0° have been investigated in respect of the predictive abilities of statistical and hybrid turbulence modelling. The DDES simulations displayed a rich content of resolved flow structures and provided a strongly detached flow and a large shock amplitude, extended from the leading to the trailing edge. This behaviour has been analysed and discussed in respect of the MSD and eddy-viscosity levels induced by this modelling associated to the present grid and numerical parameters. The URANS simulations based on the $k-\omega$ SST model have indicated a high turbulence diffusion level and a decrease in the appearance of instabilities past the trailing edge, as well as a short shock amplitude. The OES approach provided an intermediate behaviour between the two mentioned with a reasonably extended shock amplitude and capturing of the von Kármán and shear-layer vortices downstream of the SWBLI and of the trailing edge. In a study in progress, the association of DDES with OES will be examined in order to take relative benefits from both approaches.

Acknowledgements

The present work was supported by the TFAST European project No. 265455—Transition location effect on shock-wave/boundary-layer interaction. The research team thankfully acknowledges the French computing centres CINES (Centre informatique national de l'enseignement supérieur) and CALMIP (Calcul en Midi-Pyrénées) for the allocated resources as well as for their availability. They thank Matteo Bernardini and Sergio Pirozzoli for their valuable discussions about the turbulence modelling behaviour in the context of the TFAST collaboration.

References

[1] J.B. McDevitt, L.L. Levy Jr., G.S. Deiwert, Transonic flow about a thick circular-arc airfoil, AIAA J. 14 (5) (1976) 606–613. http://dx.doi.org/10.2514/3.61402.
[2] H.L. Seegmiller, J.G. Marvin, L.L. Levy Jr., Steady and unsteady transonic flow, AIAA J. 16 (12) (1978) 1262–1270. http://dx.doi.org/10.2514/3.61042.
[3] L. Jacquin, P. Molton, S. Deck, B. Maury, D. Soulevant, Experimental study of shock oscillation over a transonic supercritical profile, AIAA J. 47 (9) (2009) 1985–1994. http://dx.doi.org/10.2514/1.30190.
[4] B.H.K. Lee, Oscillatory shock motion caused by transonic shock boundary-layer interaction, AIAA J. 28 (5) (1990) 942–944. http://dx.doi.org/10.2514/3.25144.
[5] D. Szubert, F. Grossi, A. Jimenez Garcia, Y. Hoarau, J.C.R. Hunt, M. Braza, Shock-vortex shear-layer interaction in the transonic flow around a supercritical airfoil at high Reynolds number in buffet conditions, J. Fluids Struct. 55 (2015) 276–302. http://dx.doi.org/10.1016/j.jfluidstructs.2015.03.005.
[6] S. Deck, Numerical computation of transonic buffet over a supercritical airfoil, AIAA J. 43 (7) (2005) 1556–1566. http://dx.doi.org/10.2514/1.9885.
[7] F. Grossi, M. Braza, Y. Hoarau, Prediction of transonic buffet by delayed detached-eddy simulation, AIAA J. 52 (2014) 2300–2312. http://dx.doi.org/10.2514/1.J052873.
[8] L. Jacquin, P. Molton, S. Deck, B. Maury, D. Soulevant, An experimental study of shock oscillation over a transonic supercritical profile, in: 35th AIAA Fluid Dynamics Conference and Exhibit, Toronto, Ontario, Canada, 2005, AIAA 2005-4902. http://dx.doi.org/10.2514/6.2005-4902.
[9] Cleansky European project, Call 11 - GRA-02-019, Advanced, high aspect ratio transonic laminar wing for regional aircraft with load controll & alleviation devices (2013–2016).
[10] M. Belisle, M. Roberts, T. Williams, M. Tufts, A. Tucker, W. Saric, H. Reed, A transonic laminar-flow wing glove flight experiment: Overview and design optimization, in: 30th AIAA Applied Aerodynamics Conferenceth AIAA Applied Aerodynamics Conference, New Orleans, LA, 2012. http://dx.doi.org/10.2514/6.2012-2667.
[11] A. Bouhadji, M. Braza, Organised modes and shock–vortex interaction in unsteady viscous transonic flows around an aerofoil: Part I: Mach number effect, Comput. & Fluids 32 (9) (2003) 1233–1260. http://dx.doi.org/10.1016/S0045-7930(02)00100-7.
[12] S. Bourdet, A. Bouhadji, M. Braza, F. Thiele, Direct numerical simulation of the three-dimensional transition to turbulence in the transonic flow around a wing, Flow Turbul. Combust. 71 (1–4) (2003) 203–220. http://dx.doi.org/10.1023/B%3AAPPL.0000014932.28421.9e.
[13] L.L. Levy Jr., Experimental and computational steady and unsteady transonic flows about a thick airfoil, AIAA J. 16 (6) (1978) 564–572. http://dx.doi.org/10.2514/3.60935.
[14] P.R. Spalart, W.-H. Jou, M. Strelets, S.R. Allmaras, Comments on the feasibility of LES for wings, and on a hybrid RANS/LES approach, in: C. Liu, Z. Liu (Eds.), Advances in LES/DNS, Greyden Press, Louisiana Tech. University, 1997, pp. 137–147.
[15] P.R. Spalart, S. Deck, M.L. Shur, K.D. Squires, M.K. Strelets, A. Travin, A new version of detached-eddy simulation, resistant to ambiguous grid densities, Theor. Comput. Fluid Dyn. 20 (6) (2006) 181–195. http://dx.doi.org/10.1007/s00162-006-0015-0.
[16] M.L. Shur, P.R. Spalart, M.K. Strelets, A.K. Travin, A hybrid RANS-LES approach with delayed-DES and wall-modelled LES capabilities, Int. J. Heat Fluid Flow 29 (6) (2008) 1638–1649. http://dx.doi.org/10.1016/j.ijheatfluidflow.2008.07.001.
[17] J.D. Crouch, L.L. Ng, Variable N-factor method for transition prediction in three-dimensional boundary layers, AIAA J. 38 (2) (2000) 211–216. http://dx.doi.org/10.2514/2.973.
[18] P.L. Roe, Approximate Riemann solvers, parameter vectors, and difference schemes, J. Comput. Phys. 43 (2) (1981) 357–372. http://dx.doi.org/10.1016/0021-9991(81)90128-5.
[19] B. van Leer, Towards the ultimate conservative difference scheme. V. A second-order sequel to Godunov's method, J. Comput. Phys. 32 (1) (1979) 101–136. http://dx.doi.org/10.1016/0021-9991(79)90145-1.
[20] F.R. Menter, Two-equation eddy-viscosity turbulence models for engineering applications, AIAA J. 32 (8) (1994) 1598–1605. http://dx.doi.org/10.2514/3.12149.
[21] R. Bourguet, M. Braza, G. Harran, R. El Akoury, Anisotropic organised eddy simulation for the prediction of non-equilibrium turbulent flows around bodies, J. Fluids Struct. 24 (8) (2008) 1240–1251. http://dx.doi.org/10.1016/j.jfluidstructs.2008.07.004.
[22] P.R. Spalart, C.L. Rumsey, Effective inflow conditions for turbulence models in aerodynamic calculations, AIAA J. 45 (10) (2007) 2544–2553. http://dx.doi.org/10.2514/1.29373.
[23] D.R. Jones, M. Schonlau, W.J. Welch, Efficient global optimization of expensive black-box functions, J. Global Optim. 13 (4) (1998) 455–492. http://dx.doi.org/10.1023/A:1008306431147.
[24] J. Sacks, W.J. Welch, T.J. Mitchell, H.P. Wynn, Design and analysis of computer experiments, Statist. Sci. 4 (4) (1989) 409–423. URL: http://www.jstor.org/stable/2245858.
[25] V. Picheny, D. Ginsbourger, Y. Richet, Noisy expected improvement and on-line computation time allocation for the optimization of simulators with tunable fidelity, in: 2nd Int. Conf. on Engineering Optimization, 2010.
[26] B.H.K. Lee, Self-sustained shock oscillations on airfoils at transonic speeds, Prog. Aerosp. Sci. 37 (2) (2001) 147–196. http://dx.doi.org/10.1016/S0376-0421(01)00003-3.
[27] Y.C. Fung, An Introduction to the Theory of Aeroelasticity, Dover, 2002, Schlieren picture page 313 by D.W. Holder, National Physical Laboratory, England.
[28] W.J. Duncan, L. Ellis, C. Scruton, First report on the general investigation of tail buffeting, British Aeronautical Research Committee R&M-1457 1457 (1932) Part I.
[29] S. Deck, Recent improvements in the zonal detached eddy simulation (ZDES) formulation, Theor. Comput. Fluid Dyn. 26 (6) (2012) 523–550. http://dx.doi.org/10.1007/s00162-011-0240-z.
[30] A. Uzun, M.Y. Hussaini, An application of delayed detached eddy simulation to tandem cylinder flow field prediction, Comput. & Fluids 60 (2012) 71–85.
[31] C. Mockett, M. Fuchs, A. Garbaruk, M. Shur, P. Spalart, M. Strelets, F. Thiele, A. Travin, Two non-zonal approaches to accelerate rans to LES transition of free shear layers in DES, in: Progress in Hybrid RANS-LES Modelling, in: Notes on Numerical Fluid Mechanics and Multidisciplinary Design, vol. 130, Springer, 2015, pp. 187–201.
[32] F. Grossi, Physics and modeling of unsteady shock wave/boundary layer interactions over transonic airfoils by numerical simulation (Ph.D. thesis), INP Toulouse, 2014, URL: http://ethesis.inp-toulouse.fr/archive/00002643.
[33] D. Szubert, F. Grossi, Y. Hoarau, M. Braza, Hybrid RANS-LES and URANS simulations of a laminar transonic airfoil, in: Progress in Hybrid RANS-LES Modelling, College Station, TX, 2014, pp. 329–343. http://dx.doi.org/10.1007/978-3-319-15141-0.